Research Article

Plasmon Properties of Polydisperse Aluminum Nanoparticles Produced in Spark Discharge

Olesya Vershinina*, Anna Lizunova, Egor Khramov, Emiliia Filalova, Arina Sanatulina, Artem Novoselov, Messan Nouraldeen, Dana Malo, Ekaterina Kameneva, Mariia Kerechanina, Yuri Tokunov and Victor Ivanov
Moscow Institute of Physics and Technology, National Research University, Dolgoprudny, Russia

* Corresponding author. E-mail: seraia.ov@phystech.edu DOI: 10.14416/j.asep.2025.02.001
Received: 24 September 2024; Revised: 18 November 2024; Accepted: 14 January 2025; Published online: 7 February 2025

Abstract
Nanoscale aluminum is a promising material for ultraviolet (UV) plasmonics for improving biosensors, light sources, and solar cells. Our study proposes a technique for producing aluminum nanoparticles with controlled average sizes using a gas discharge by adjusting the energy density released on the electrode surfaces. The key objective of this research is to investigate the impact of the variation in the dimensions of the inner and outer diameters of the electrodes on the synthesis efficiency, size distribution, and optical properties of primary nanoparticles, and to theoretically predict their potential for metal-enhanced luminescence applications. The morphology and structure of the resulting polydisperse nanoparticles were analyzed with transmission electron microscopy (TEM) and energy-dispersive X-ray spectroscopy (EDX). An increase in the average size from 15 to 26 nm and up to 7-time gain in the production rate with an increase in the energy density released on the electrodes were observed. The optical absorption spectra of the aluminum core-shell particles, both theoretically calculated through the Mie theory and experimentally obtained via spectrophotometry, exhibited plasmon resonance maxima in the deep ultraviolet range, with wavelengths spanning from 208 to 237 nm. Simulations of plasmon-enhanced fluorescence indicated a strong coupling of individual emitters to the plasmonic mode of produced aluminum nanoparticles and showed the enhancement factor ranging from 2 to 85 times, which depended on the particle size distribution, the quantum yield of the phosphor, the metal-emitter distance, and the excitation wavelength. The findings highlight that the produced polydisperse aluminum nanoparticles enhance emitter performance in the UV range, providing prospects for advancing optoelectronic devices.

Keywords: Core-shell aluminum nanoparticles, Metal enhanced luminescence, Plasmon properties, Spark discharge, Ultraviolet

1 Introduction

Aluminum stands out as an abundant, cost-effective, and environmentally safe material highly compatible with optoelectronic devices. In its nanosized form, aluminum exhibits high reactivity and proves invaluable across diverse applications such as energetics, hydrogen storage, biomedicine, aluminum-based batteries, photocatalysis, energetics and photonics [1]–[7]. A naturally occurring oxide film covering aluminum nanoparticles, grants them stability and protection against combustion, while maintaining minimal cytotoxicity thanks to the inert nature of the aluminum oxide surface [8], [9]. Previous research has shown that aluminum core-shell nanoparticles at concentrations of 25 μg/mL do not impair cellular viability and that aluminum oxide nanoparticles under 100 nm demonstrate antibacterial effects against Staphylococcus aureus [10].

The phenomenon of localized surface plasmon resonance (LSPR) in metal nanoparticles significantly enhances electromagnetic fields, making them attractive for plasmonics research [11], [12]. Numerous studies have explored the synthesis and applications of gold and silver nanoparticles to form plasmonic microstructures and devices functioning in

the visible and infrared spectrum. These nanoparticles significantly enhance luminescence and SERS (Surface-enhanced Raman spectroscopy) signals [13], [14], ameliorate sensitivity of bio-, gas- and optical-sensors [14], solar cells [15], [16] and catalyst agents [17].

However, gold and silver nanoparticles present challenges such as high optical losses, incompatibility with silicon manufacturing, and the degradation of silver upon air exposure [18], [19]. By contrast, ultradispersed aluminum nanoparticles exhibit strong plasmon resonance primarily in the ultraviolet and blue visible regions, and demonstrate high atmospheric stability due to the formation of a protective oxide layer [20]–[23].

Although metals such as Mg, Pt, Ga, In, and Rh also offer UV plasmonic properties [24], aluminum attracts attention for its low cost, abundance, stability, and non-toxicity, making it a promising material for UV plasmonic devices [20], [25]–[28]. Synthesizing aluminum nanoparticles presents considerable challenges due to their unique physical and chemical properties [28]. While numerous methods exist [27], such as wet chemistry, electron lithography, molecular beam epitaxy, and electric wire explosion, all of them have limitations and drawbacks. For instance, wet chemistry approaches are complicated by the chemical instability of aluminum in colloidal forms [29]–[31]. Substrate methods like molecular beam epitaxy and electron beam lithography, offer high reproducibility and quality but are hindered by cost, complexity, and limitations on achieving small particle sizes [20], [32]–[34].

Nanoparticles generated by gas-phase methods, including pulsed laser ablation, arc and spark discharge, electric wire explosion, and electromagnetic levitation gas condensation [35]–[39], are beneficial for developing planar plasmonic devices, using techniques like spraying, electrostatic deposition, spin coating, and inkjet printing from liquid colloids [40]–[43]. Among these, the gas discharge method is particularly advantageous [22], [43]–[45]. This method enables the direct deposition of high-purity nanoparticles through a focused nozzle onto substrates without requiring liquid-phase processing, making it a cost-effective and environmentally friendly option that requires only energy and electrode materials with a specific electricity consumption ranging from 0.037 to 7 kWh/g [46]–[48]. The gas discharge method produces high-purity aerosol nanoparticles as submicron agglomerates. The primary nanoparticle size, ranging from 5 to 15 nm, depends only on the electrode material's properties rather than electrical circuit parameters [49], [50]. Achieving larger sizes (50–150 nm) requires extra in-flow thermal or laser treatments, which are ineffective for aluminum owing to its oxide shell's high melting point [51], [52].

Based on the findings that electrode asymmetry can affect size distributions, as proposed in studies with silver nanoparticles [53], our research explores an alternative approach to increase primary particle sizes by altering the geometry of the electrodes. This exploration could enhance the synthesis of aluminum nanoparticles, overcoming limitations faced in current methodologies. The particle size, morphology, shape, and structure play a crucial role in the plasmonic properties of metals. Aluminum nanoparticles with different sizes reveal resonant oscillation of conduction electrons in a large-scale ultraviolet (UV) spectral range and thus can be effective in enhancing light-matter interactions for different applications [54], [55].

Synthesis of Al NPs with a diameter of 5–60 nm, which exposes resonance absorption in a range of 150–300 nm, according to Mie simulations, is an actual task for UVC and UVB plasmonics. For example, it is an intriguing challenge for biological sensing without using extra dye fluorescent labeling because many biological fluids, such as amino acids and proteins, have fluoresce in UV below 300 nm [54], [56]–[58]. Also, this UV region is an active area of research to improve the solar cell efficiency and enhance internal quantum efficiency and electroluminescence of AlGaN LEDs in the deep UV range [59], [60].

Our study aimed to investigate the particle size distribution, shape, morphology, and optical properties of primary aluminum nanoparticles produced within a gas discharge by altering the erosion area of electrodes, specifically by adjusting their inner and outer diameters, as the characteristics of the electrical circuit have no impact on the dimensions of the primary particles. Moreover, to figure out the potential applications of the acquired particles, our research proceeded to theoretical computations of the luminescence enhancement factor for ultraviolet emitters in the vicinity of polydisperse aluminum particles, with particle size distributions resembling those observed in the experiments.

2 Materials and Methods

2.1 *Spark discharge setup*

Aluminum nanoparticles were obtained using a gas discharge generator developed by our laboratory, containing a high voltage source, an energy storage device (a capacitor with a capacity of 107 nF), and a T-shaped chamber. Figure 1(a)–(c) illustrate a gas discharge setup schematic image, configurations of the used electrodes, and a nanoparticles generator photograph, respectively.

Nanoparticle synthesis is based on the simultaneous erosion of two oppositely facing cylindrical aluminum electrodes, resulting from the interaction of the spark and flat metal surface. The high voltage applied to the electrodes caused gas breakdown, leading to the formation of a conductive channel with subsequent dissociation and ionization of gas molecules. The duration of the discharge is characterized by several microseconds, which is sufficient to locally heat the electrodes to high temperatures of 20000–40000 K, based on the calculations [61]. Then, the material from the electrode surface began to evaporate, forming a vapor-liquid dispersion. The rapid cooling in an inert gas at a temperature below the boiling point provoked metal supersaturation and nucleation, forming metal nanoparticles. A continuous carrier gas flow passing through one of the hollow electrodes entrained the nanoparticles from the gap and conveyed them along the path, promoting their further agglomeration.

The electrodes were installed opposite each other at a fixed inter-electrode gap of 1.5 mm. The carrier gas flow of 50 mL per min, the repetition rate of 500 Hz, and a discharge voltage of 1.6 kV were used to generate aluminum nanoparticles. To avoid oxidation of metal, the argon 6.0 gas was used during synthesis. The subsequent passivation was carried out in an argon 4.8 atmosphere to cover the surface of the metal nanoparticles with a native oxide shell, protecting them from potential explosion.

The electrodes were carefully polished, cleaned, and weighed on high-precision Secura 225D-1ORU scales (Sartorius Inc., Germany). The aerosol flow of synthesized nanoparticles was directed to three outputs: a TEM copper grid covered by an amorphous carbon film, a cellulose filter, and a Scanning Mobility Particle Sizer (SMPS) Spectrometer Series 3938 by TSI (Figure 1(d)) to measure the agglomerate size distribution of airborne nanoparticles. The collection period depended on the production rate and varied from 10 min to 2.5 h.

The data on the size, morphology, and crystalline structure of the synthesized nanoparticles using electrodes with different internal and external diameters were obtained using a transmission electron microscope (TEM) (JEM-2100, JEOL Ltd., Tokyo, Japan) at an accelerating voltage of 200 kV. The surface of the electrodes was made using a scanning electron microscope (SEM) JEOL JSM-7001F. The electron microscopy investigations were performed using equipment of the MIPT Shared Facilities Center.

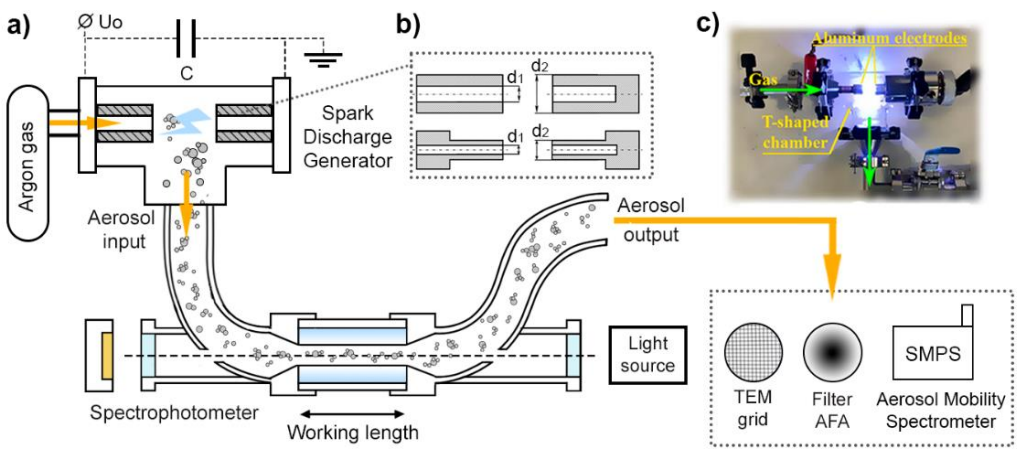

Figure 1: (a) Schematic image of the spark discharge setup with an extra chamber for aerosol absorption measurements. (b) Aluminum electrode configurations. (c) Photograph of the spark discharge setup.

The optical spectra of aerosol nanoparticles in a wavelength range of 250–1000 nm were obtained using an HR4000CG-UV-NIR spectrophotometer (Ocean Insight, Orlando, FL, USA) with a light input from a white light source (halogen lamp) through an optical fiber installed at the entrance to the laser optimization cell at the position of the light source. Production rate measurements were performed by weighting the mass of electrode pairs before and after the synthesis process and dividing the discrepancies by the operating time of the electrode.

Colloids for optical density measurements were made by mixing the obtained aluminum nanoparticles with chromatographic pure isopropanol (Sharlau). The optical density spectra of the suspensions were measured on a JASCO V-770 (Jasco, Japan, Tsukuba) UV-Visible/NIR spectrophotometer in quartz cuvettes (Thorlabs, Newton, NJ, USA) with an optical path length of 1 cm. The measurements were made with correction on the "100% transmission" baseline and with subtraction of the absorption of the solvent.

2.2 *Electrodes*

In the beginning, we developed a scheme of cylindrical electrodes with a different configuration and a diameter made of 99.9999% pure bulk aluminum. We ground aluminum electrodes with flat ends in two principal geometries shown in Figure 1(b). Figure 2(b) provides real photos of the first type of experimental electrodes after the erosion process in a spark discharge. The electrodes have a fixed outer diameter d_2 8 mm and a variable inner diameter d_1 in a range from 2 to 6 mm (namely, 2, 3.5, 4.5, 5.3, and 6 mm). In the second experiment, the outer diameter d_2 was changed from 8 to 4 mm (specifically, 8, 7.2, 6.3, 5.3, and 4 mm); whereas the inner diameter possessed a constant value of 2 mm (Figure 2(c)). We used abbreviations *In* for the inner diameter and *Ex* for the external diameter value. By adjusting the diameters of the electrodes, we achieved the difference in the surface area of the erosion material and a distance of the electrode material from the center of symmetry. When the surface area of the electrode erosion changed, the energy density reaching the electrode surface shifted as well. The relationship between the geometry of the electrodes and the energy density is shown in Table 1, recalculated, according to the energy stored in the capacitor 107 nF and a voltage in the interelectrode gap of 1.6 kV. Decreasing the erosion surface of the electrodes, responsible for the spark synthesis, led to an increase in energy density, thus altering the synthesis productivity (Figure 2(d)).

The dependence of the microstructure of the electrode surface after erosion on energy density is shown in the SEM images in Figure 2(a). A noticeable reduction in the size of molten material droplets and craters occurred as the energy density decreased.

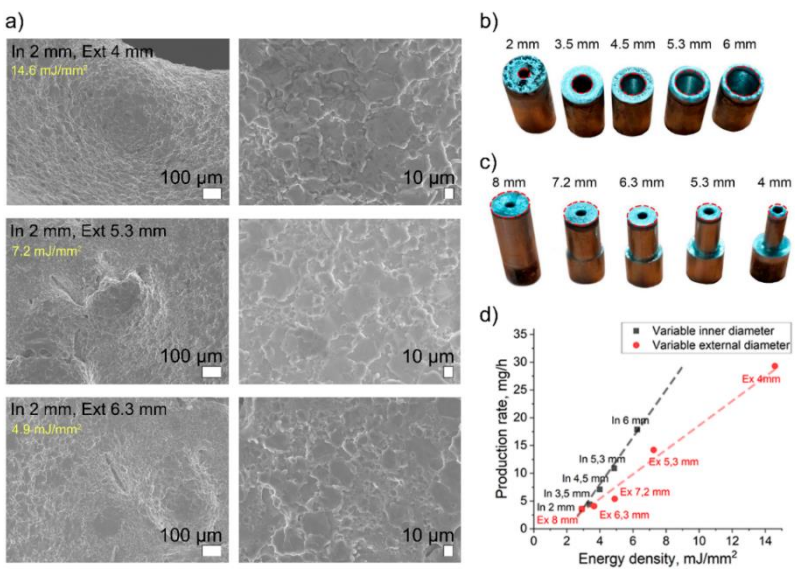

Figure 2: Study of the electrode end surface. (a) SEM images of three cathodes undergoing spark discharge erosion with different energy densities; photographs of the electrodes with different geometrical configurations (b) Type 1 configuration of the electrodes, fixed outer diameter 8 mm and variable inner one, and (c) Type 2 configuration, fixed inner diameter 2 mm, (d) dependence of the production rate via energy density.

Table 1: Dimensional and optical properties of obtained Al nanoparticles.

Type of Electrodes	Changeable Diameter Size (mm)	Erosion Area (mm^2)	Energy Density (mJ/mm^2)	Production Rate (mg/h)	Average Diameter of Primary NPs (nm) (TEM)	Experimental Plasmon Peak Position (nm)	Calculated Peak Position (nm)
Fixed outer diameter of 8 mm	6	21.9	6.3	17.9	23.8 ± 14.4	236.7	223.5
	5.3	28.2	4.9	10.9	21.9 ± 10.6	235.2	219.3
	4.5	34.4	4.0	7.1	17.2 ± 7.5	232.0	220.8
	3.5	40.6	3.4	4.4	14.9 ± 6.2	212.0	219.1
	2	47.1	2.9	3.6	15.2 ± 5.4	215.2	218.9
Fixed inner diameter of 2 mm	4	9.4	14.6	29.3	26.4 ± 13.4	232.4	224.0
	5.3	18.9	7.2	14.2	18.7 ± 9.4	235.2	219.7
	6.3	28.0	4.9	5.4	16.9 ± 5.3	210.9	219.5
	7.2	37.6	3.6	4.1	15.2 ± 5.8	208.4	218.9

3 Results and Discussion

3.1 *Production rate study*

Figure 2(d) and Table 1 show that the geometry of electrodes strongly influences the production rate of nanoparticles in spark discharge. The graph depicts the relationship between energy density (in mJ/mm^2) and production rate (in mg/h) for spark discharge synthesis, comparing two electrode configurations: Type 1, variable inner diameter (black squares) and Type 2, variable external diameter (red circles). The data points represented by black squares show a more pronounced increase in production rate with increasing energy density.

The graph is approximated by a linear function between the mass loss of electrode material and energy density. That means that the higher the energy density, or the amount of energy stored in the capacitor and released in the interelectrode gap per end surface area of the electrodes, the greater the mass loss of the electrodes.

Also, there is an obvious trend in the productive rate of spark discharge synthesis depending on the type of electrode configurations. At a constant energy density, the value of synthesis productivity is higher for electrodes with variable inner diameter. The slope of the fitting black and red lines distinguishes 1.9 times, suggesting that varying the inner diameter of the electrodes (Figure 2(b)) has a more substantial effect on improving the production rate at the constant energy density compared to modifying the external diameter (Figure 2(c)).

This result means that the erosion process proceeds nonuniformly, and the electrode material is removed more from the outer area of the end electrode located far away from the symmetry axis of the electrode. What is remarkable about the further application of thin-walled cylindrical electrodes with a large hole diameter (Figure 2(b)) is the improvement in the production efficiency at the same pulse energy. So, for example, the energy density of the spark is constant and equal to 5 mJ/mm^2. When it is released in the electrode type shown in Figure 2(c), the productivity rate is 7.4 mg/h, but the electrode type shown in Figure 2(b) allows for 14 mg/h of nanopowder production. Thus, by focusing on changing the electrode geometry, one can achieve a more than 90% increase in productivity only by increasing the width of the hole in the electrode.

By increasing the energy density five times from 2.9 to 14.6 mJ/mm^2, one can expect a threefold improvement in the production rate. Herewith, we achieved an enormous range of production rate from 3.6 to 29.3 mg/h (approximately 8 times) only by altering the surface area of the electrodes at uniform values of parameters of an electrical circuit, gas flow, pressure, and frequency of discharge. It was recently shown that the electrode mass loss depends on the distance between the electrodes and the angle of the bevel between electrodes [53]. The production rate of Al nanoparticles obtained in our study is similar to other metal and semiconductor materials produced in spark discharge. Nobel metals, such as gold and silver, and semiconductor materials, namely, germanium and silicon, possess a lower production rate of 10–30 mg/h; whereas tin electrodes have greater erosion in spark discharge and results in the production rate of up to 1 g/h [49], [62]–[64].

3.2 *Morphology and structure of nanoparticles*

Investigation of Al nanoparticles by transmission electron microscopy revealed considerable influence of energy density on the size and dispersity of nanoparticles. The representative TEM images of agglomerates of aluminum nanoparticles are shown in Figure 3(a)–(e) in order of increasing energy density values from 2.9 to 14.6 mJ/mm^2. The images reveal an

increase in the nanoparticle size, with the appearance of large particles reaching 125 nm, with the external electrode diameter being 4 mm and the maximum energy density being 14.6 mJ/mm^2. Our study reveals that the particle shape is close to spherical, oval, and complex roundish. All particles exhibit a core-shell structure, as seen in Figure 3(g). The high-resolution TEM images and elemental EDX analysis (Figure 3 (k)–(o)), including mapping of individual particles and line profile of elements, confirm that the shell is amorphous and consists of an aluminum oxide phase. The thickness of the shell is non-uniform and varies from 2.5 to 5.0 nm from particle to particle. We measured that the aluminum oxide shell has an average thickness of about 4 nm, which covered the metal core of each nanoparticle. We suggest that the shell is forming during the passivation process in argon 4.8, which contains 0.001% nitrogen gas and only 0.001% of oxygen and water vapor in total. However, the tiny amount of residual oxygen in the argon environment appears to be sufficient to interact with the reactive surface of ultrafine metal aluminum nanoparticles and clothe them with an oxide shell. Under normal conditions, the obtained shell remains stable when nanoparticles are stored in powder or non-aqua solution. Our previously conducted experiments showed the long-term sustainability of the average thickness of the shell for several years for Al nanoparticles produced in gas discharge and electric explosion of wires [56]. Many researchers detected a thin oxide film of 2–5 nm on Al NPs produced by electron lithography or electric explosion of wires upon exposure to air [65]–[67]. Oxidation of the surface of Al NPs stops at a critical moment when the formed oxide shell can protect against penetration of additional oxygen inside the metal core. Increasing the thickness of the oxide shell is possible only during heating at high temperatures in an oxygen atmosphere [68].

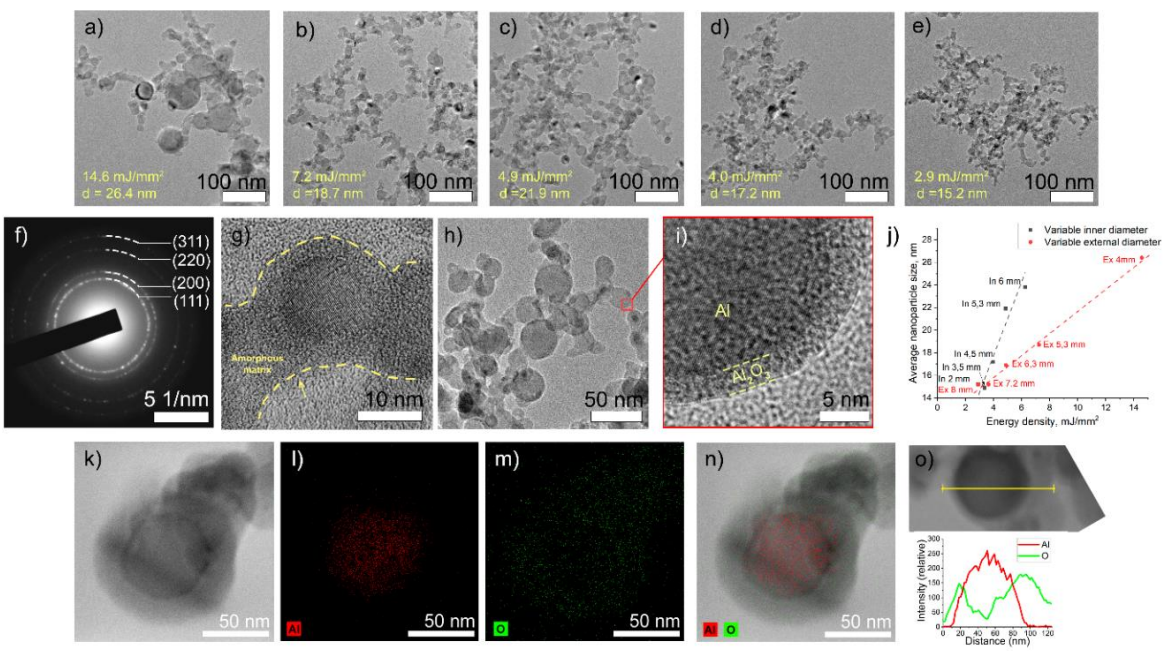

Figure 3: TEM images of aluminum agglomerates produced in spark discharge using different electrodes' geometry with increasing energy density: inner diameter of electrode 2 mm and external diameters of (a) 4 mm and (b) 5.3 mm, and external diameter of 8 mm and inner diameters of (c) 5.3 mm, (d) 4.5 mm and (e) 2 mm, (f) diffraction pattern of nanoparticle ensemble, (g) Al NP in an amorphous matrix (yellow bounds), (h) zoomed TEM images of sample c); (i) HRTEM image of core-shell nanoparticles structure, (j) dependence of average size of primary nanoparticles via the energy density. Representative images of the Al@Al_2O_3 core-shell NPs obtained in spark discharge (STEM-EDX, mapping tool): (k) direct scanning electron image; distribution of aluminum (l) and (m) oxygen inside the particle, (n) overlapping of the signals detected from aluminum (red color) and oxygen atoms (green color), (o) normalized line scan profile of the corresponding Al@Al_2O_3 core-shell NP.

As presented in the TEM images (Figure 3) primary particles formed huge fractal agglomerates. Figure 3(g) shows amorphous aluminum oxide necks between primary particles connecting particles into fractals. Agglomeration is typical of many vapor-phase processes as spark and arc-discharge, pulse laser ablation, and electrical erosion of wire. According to the paper, the primary particle is a coalescent unit, formed from vapor between electrodes during the collision and coalescence of atoms, then primary particles constitute the agglomerates [69].

Electron diffraction patterns confirmed the crystalline structure of the core. A typical SAED (selected area electron diffraction) pattern of the agglomerates (an ensemble of Al NPs) is shown in Figure 3(f) and indicates that all rings corresponded to the diffraction planes of metal aluminum Fm3m space group, with interplanar distances of 2.3380 Å (111), 2.0248 Å (200), 1.4317 Å (220), 1.2210 Å (311), and 1.1690 Å (222). Each nanoparticle is monocrystalline, as presented in Figure 3(g) and (i). The SAED was obtained from an ensemble of multidirectional monocrystalline Al NPs, where each pair of point reflexes corresponding to a signal from a monocrystalline particle forms rings on the diffraction pattern.

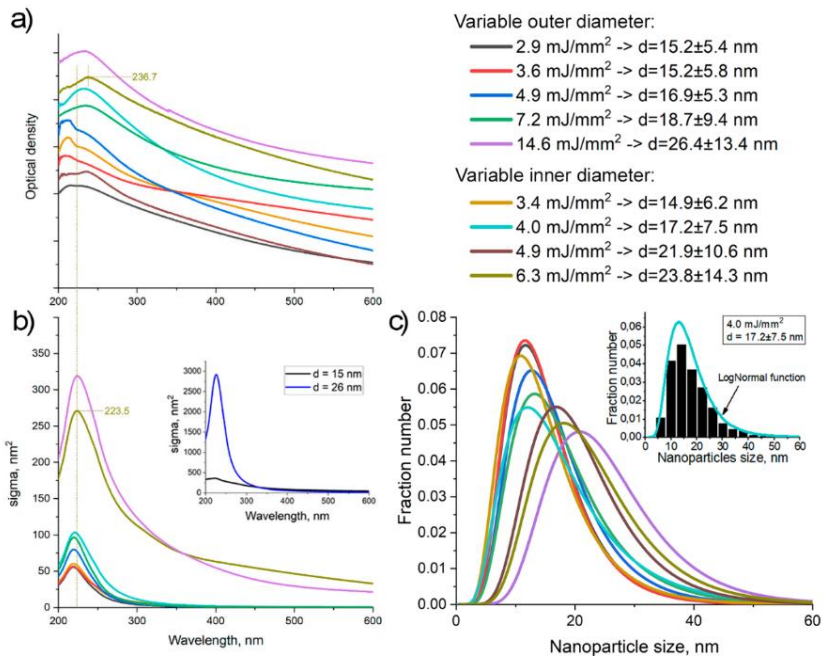

Figure 4: Optical properties of the obtained aluminum nanoparticles depending on different electrode diameters. (a) The experimental optical density of NPs in liquid dispersions. (b) Simulated cross-sections according to the Mie theory (the lower part) and simulated spectra for monodisperse particles with diameters of 15 and 26 nm (the insert). (c) Approximated by log-normal curves size distribution of nanoparticles. The inserted size distribution corresponds to the particles obtained from electrodes with an inner diameter of 4.5 mm and an outer diameter of 8 mm.

The average particle size was estimated by analyzing a sample of 1000 particles characterized by a specific equivalent diameter, which evaluates the area of each particle. The data on the average size of nanoparticles obtained at a specific energy density (electrode diameters) are presented in Table 1. The distributions of primary particle diameters are demonstrated in Figure 4(c) (insert). The particle distributions are well approximated by a log-normal function (Figure 4(d)), and the width of the distribution broadens as the energy density increases. At low energy density, the particle size distribution is narrow, with an average size of 15.2 ± 5.4 nm. However, raising energy density to its maximum value broadens the distribution and increases average particle sizes to 26.4 ± 13.4 nm. Furthermore, the samples contain single large particles with a size of 180 nm and an energy density greater than 6.3 mJ/mm^2.

Figure 4(c) (insert) shows the particle size distribution obtained for an energy density of 4.0

mJ/mm^2, applied to the electrodes, which clearly illustrates the polydisperse ensemble of NPs. Although the average particle size is quite small (17.2 nm), the number of particles in a range of 5–50 nm is 92%, also several particle diameters up to 85 nm are present.

Additional high-temperature (up to 1000 °C) sintering of spark discharge agglomerates in the gas stream reshapes them into massive individual nanoparticles through melting and coalescence of small primary particles [52]. However, the aluminum oxide shell covering the metal core possesses a high melting point (~ 1600 °C); whereas the maximum temperature of our furnace is 1000 °C, so our equipment does not allow modifying agglomerates of Al NPs with an oxide shell to large individual NPs. So, the creation of high-potential methods to change the particles size is important for the development of a spark generation technique.

Our thorough analysis of Table 1 reveals a direct correlation between the size and production rate of synthesis. In the case of the growth of electrodes' mass loss during erosion, the average particle size of the produced nanoparticles also expands. We attribute this effect to the physical mechanism of particle creation in the spark discharge. The electrode material is vaporized in the vicinity of the spark due to plasma that emerges in the channel between the electrodes. Clusters of aluminum formed from vapor during diffusion-driven nucleation consolidate and condense into primary nanoparticles. In the case of a high concentration of clusters confined to a limited gap, the likelihood of collisions increases, resulting in the creation of larger primary nanoparticles. Whereas the productivity is low, clusters rarely come into contact, resulting in the synthesis of tinier nanoparticles.

3.3 *Study of the optical properties of nanoparticles*

We found that the experimental extinction spectra (Figure 4) of Al agglomerates in colloids in isopropanol (chromatographic purity, LiChrosolv) are characterized by discernably pronounced peaks in a UV wavelength range of 208–237 nm, with weak dependence of its positions on the size of primary nanoparticles. The experimental absorption peaks observed for all samples are provided in Table 1 with values within the UV-range. The absorption peak with redshift was found to be broader as the size distribution became wider.

The red, black, beige, and blue curves represent ensembles of tiny nanoparticles with the lowest mode of 11–13 nm and a narrow distribution breadth (Figure 4(a)). For these NPs ensembles, we detected a principal surface Plasmon resonance peak at a wavelength of 210 nm, and a weak bump located around 235 nm, which we attribute to agglomerates, as it does not occur in the calculated spectra (Figure 4(b)). As the fraction of large particles appears (shown by blue, brown, green, and violet colors on the curve, with the distribution mode located at 17–21 nm), the absorption resonance peak shifts to longer wavelengths by 13–22 nm, now ranging from 223 nm to 237 nm. Additionally, the expansion of the particle size distribution causes enlarging the width of the resonance peak. The appearance of individual large particles with diameters ranging from 60 to 120 nm, observed in the samples represented by violet and olive curves, leads to the appearance of a weak peak in the calculated spectrum around 246 nm and 311 nm, as well as significant broadening of the absorption spectrum. Furthermore, the broadening of the peaks and their shift towards longer wavelengths can be attributed to the presence of larger particles, since an increase in the size of monodisperse particles results in a shift of absorption peak to the visible range and the formation of agglomerates [56], [70], [71].

3.4 *Study of the optical properties of nanoparticles*

In accordance with the Mie theory, a physicomathematical model was implemented to calculate the extinction cross-sections of polydisperse spherical aluminum nanoparticles. Spectra were calculated for nanoparticle ensembles with a lognormal size distribution obtained by TEM for aerosol Al-nanoparticles of the core-shell structure with an aluminum core and dielectric Al_2O_3 shell with a constant thickness of 4 nm. The ambient medium was isopropyl and we suggested that particles do not interact with each other, namely, there are no agglomerates.

It was established that the spectra (Figure 4) are characterized by a clearly defined peak ranging from 218 to 224 nm. The theoretical spectra slightly shift to longer wavelengths as the average size increases from 15 to 26 nm. The obtained values of the Plasmon maximums for each sample are presented in Table 1. Despite approximately the same positions of the local maxima of the plasmon resonance at a wavelength of about 220 nm, an enlarging of the peak is observed, which is associated with the appearance of large particles in distribution. Weak peaks located at 275 and 322 nm were observed for broad particle size distribution (olive curve).

Several research groups investigating monodispersed aluminum nanoparticles obtained absorption spectra both experimentally and theoretically [21], [22], [33], [56] [72]–[75]. In all cases, a plasmon resonance was observed in the ultraviolet range, and as the particle diameter increased, a shift of the plasmon resonance peak into the infrared range with broadening was observed.

Theoretical absorption spectra for aluminum core-shell nanoparticles with varying core diameters and shell thicknesses were computed using the Mie absorption theory by Hu *et al*. [21]. For instance, with a particle diameter of 10 nm and an increase in the shell thickness from 0 to 10 nm, a redshift of the plasmon resonance peak from 150 to 230 nm was observed, along with broadening. In the case of monodisperse particles larger than 25 nm, in addition to the one dipole mode, quadrupole and octupole modes were expressed in the extinction spectra. Absorption efficiency spectra for Al nanoparticles greater than 10 nm in diameter show quadrupole and octupole resonance, shifting the dipole mode to the UV-A region for NPs larger than ~80 nm [56], [75]. Furthermore, for polydisperse systems, the dipole mode moves to the visible range when the size increases above 60–80 nm, but it is smoothed out during averaging with different weight coefficients, leaving just a broadened peak in the UV, [56], [71]. These data are also supported by our experiments.

The spectra of nanoparticles, whose synthesis was performed using laser ablation in liquid, lithography, and colloidal solutions [30], [33], [72], were subjected to comprehensive analysis. When the diameter of aluminum nanoparticles produced by physical methods increased from 10 to 140 nm, as evident from both theoretical calculations and experimental data, the plasmon absorption peaks were detected in the UV-C and shifted into the longwave region from 150 nm to 240 nm, additionally, peak profile was broadening.

3.5 *Plasmon-enhanced fluorescence calculations*

Fluorescence is an effect of photon emission whose intensity depends on the power of initial light, absorption coefficient, concentration, and quantum yield of a fluorophore (emitter). We hypothesize that, due to surface plasmon effects, the quantum yield and intensity of the electromagnetic field change drastically in the presence of metal nanoparticles; whereas the concentration and absorption coefficient of the fluorophore remain constant [11]–[14]. So, we suppose that an enhancement factor of luminescence is proportional to the boost of the local electromagnetic field and modification of quantum yield [11], [76]. In our case, the first expression of the field enhancement factor was calculated by solving the Mie scattering of linearly polarized plane electromagnetic waves on a spherical aluminum nanoparticle with a constant aluminum oxide shell. The luminescence can be amplificated only if incident field enhancement promoting a higher excitation rate is not overcome by nonradiative decay enhancement leading to quenching, theoretically expressed as quantum yield drop [55]. Formally, this can be represented in Equation (1) as the product of two multipliers:

$$F = G_E(\lambda, r)G_Q(\lambda', r). \quad (1)$$

Where $G_E(\lambda,\boldsymbol{r})$ is the intensity amplification factor of the initiating electromagnetic field with a wavelength λ, which derivates from Mie theory; $G_Q(\lambda',\boldsymbol{r})$ is the field amplification factor associated with a change in the quantum yield of the emitter with photoluminescence at the wavelength λ', and r is the radius vector of the emitter.

Quantum yield modified by the proximity of a metal nanostructure and represented as a function of intrinsic quantum yield in the absence of nanoparticles and the possibility of radiative (luminescence) and non-radiative transition (phonons) of the exited quantum system to ground state using the Equation (2):

$$G_Q = \frac{\gamma_{rad}}{\gamma_0}\left(1 + Q_0\left(\frac{\gamma_\Sigma}{\gamma_0} - 1\right)\right)^{-1}. \quad (2)$$

Where γ_0 and Q_0 are the radiative transitions rate and the quantum yield of the emitter in the absence of a nano object, respectively, and γ_{rad} and γ_Σ are the radiation and total rate of spontaneous decay.

It is known that an electron restricted in the volume of a metal nanoparticle and excited by a photon has two modes for energy relaxation: radiative, which means re-emitting of photons or non-radiative decay refers to the interband transition between energy levels without light emission. The in-depth description of the theoretical items and restrictions exploited in our simulations was derived and demonstrated by Guzatov *et al*. in the articles [55], [76].

We investigated plasmonic normalized enhanced luminescence effects based on the model of light emission by a dipole emitter near a metal aluminum

spherical polydisperse nanoparticles covered by an aluminum oxide shell in the air atmosphere. Fluorescence intensity was calculated in the ultraviolet region from 200 to 400 nm for two different phosphors: ideal (with intrinsic quantum yield Q_0=1) and low (Q_0=0.01), based on the distance between the surface of a metal nanoparticle and an emitter. The emission wavelength was fixed at 380 nm, similar to ZnO nanocrystal luminescence.

Calculations were performed for three samples with polydisperse size distributions, obtained for aluminum nanoparticles produced during the erosion of electrodes with a fixed inner diameter of 2 mm and following external ones: 7.2, 5.3, and 4 mm. These particles possess different average diameters of 15.2, 18.4, and 26.4 nm, correspondingly, and increasing width of the particle size distribution (Figure 1 red, green, and violet approximations). The specified diameters include oxide shells, whose thickness is accepted to a constant average value of 4 nm for all simulations.

Figure 5 represents a weak plasmonic photoluminescence enhancement of a perfect emitter performance (Q_0=1) in the UV with aluminum polydisperse nanoparticles. Moreover, a larger size of metal nanoparticles results in the growth of the enhancement factor from 2.0 to 3.5 (1.75 - times) and leads to achievement of maximum efficiency at shorter emitter-metal spacing.

Comparing the left and right columns in Figure 5 provides a quick understanding of how the emitter's quantum yield impacts luminescence efficiency. For a weak emitter with quantum yield 0.01, the possible plasmon-enhancement factor increases by 45–85 fold. This is due to the fact the relative contribution from metal-enhanced nonradiative decay will be insignificant as quantum yield approaches zero [55]. Prodigious 85-fold average amplification of luminescence of weak emitter (Q_0 = 0.01) at 380 nm in the presence of aluminum nanoparticles 26 nm in diameter with broad particle size distribution can be achieved using excitation wavelengths 200–230 nm while the metal particles are located 2–3 nm from the phosphor. It is known that metal–emitter spacing is crucial to prospering strong coupling between quantum emitters and surface plasmon in metal nanoparticles. The optimum spacing in a range of 2–4 and 6–12 nm are determined for perfect and poor emitters, correspondingly; whereas several groups experimentally showed that the optimal distance is located from 3 to 7 nm [77], [78].

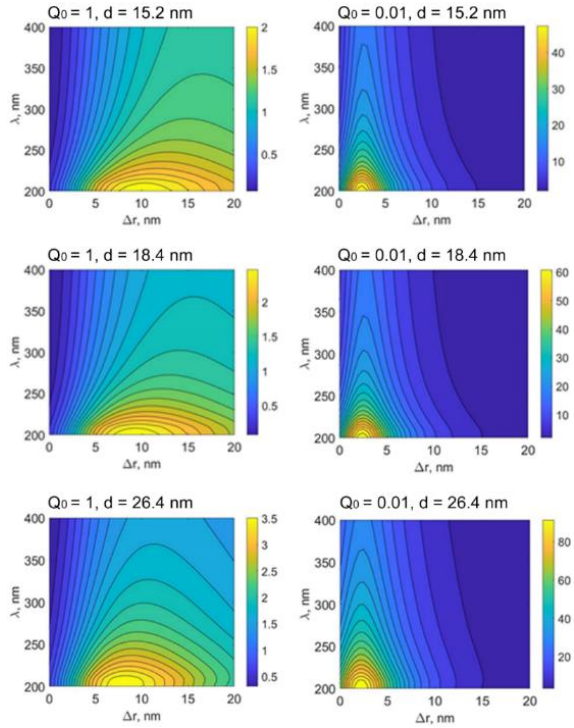

Figure 5: Calculated photoluminescence intensity enhancement factor versus excitation wavelength and metal–emitter spacing for polydisperse Al nanoparticles with different mean diameters of 15.2, 18.4, and 26.4 nm. The emission wavelength is 380 nm, and the intrinsic quantum yield of ideal phosphor Q_0 = 1 (left column) and poor emitter with Q_0 = 0.01 (right column). The calculations were done in the framework of the general Mie theory.

Notably, reported research was conducted for gold or silver nanoparticles without dielectric shells; whereas in our work, spark discharge aluminum nanoparticles possess 4 nm natural oxide coating. In addition, an approximately 2-time decrease of maximum enhancement factor can be observed whilst the mean size of metal particle drops from 26 to 15 nm. Pham *et al.* [79] obtained similar results concerning the enhancement of the electric field near polydisperse gold nanoparticles of various sizes.

Experimentally, a 1.5-fold enhancement of blue photoluminescence of $CsPbBr_{3-x}Cl_x$ in toluole was acquired in the work using aluminum nanoparticles of 20–30 nm in diameter with aluminum oxide and carbon shell [70]. Our previous experiments represented PL amplification of ZnO (377 nm) up to 3 times in colloidal mixtures with Al NPs produced by spark discharge and wire explosion methods [28],

[80]. Nanostructures based on the obtained nanoparticles with 15 nm in diameter prepared by dry aerosol printing gave an opportunity to achieve a 30 % improvement in the luminescence of zinc oxide nanocrystals in the ultraviolet range [80].

The resulting Al nanoparticles were considered an intriguing base for the development of sensing nanostructures using a dry aerosol printing technique for labeled free detection of nucleotides and antigen-antibody complexes for biotesting [81], [82], as well as the improvement of solar cells and LED efficiency in the deep and middle ultraviolet spectrum. The performance enhancement of UV photodetectors and deep UV micro-LED due to the fascinating Plasmon properties of metal aluminum nanoparticles give promising results in creating manufactured devices [83], [84].

4 Conclusions

We used calculations to demonstrate the potential application of polydisperse metal aluminum nanoparticles synthesized in a spark discharge generator for Plasmon-enhanced luminescence in the UV range. We developed an original method to adjust the size of primary nanoparticles in the spark discharge setup based on changing the geometrical configuration of electrodes used for erosion. The obtained Al nanoparticles in the form of agglomerates are defined by the average size of primary nanoparticles ranging from 15 to 26 nm, which grows with increasing energy density released on the end of the electrode. The core-shell structure of nanoparticles consists of a metal aluminum core and an amorphous aluminum oxide shell with an average thickness of 4 nm. We found that the 5-fold growth of energy density results in the production rate boosting from ~4 to ~29 mg h^{-1}. Furthermore, the geometry of the electrodes also plays a crucial role in the erosion process of the electrodes. The obtained polydisperse nanoparticles exhibit plasmon resonance in the deep ultraviolet range from 208 to 237 nm in the experimental study, as well as in the Mie calculations. According to the simulations, the presence of the obtained polydisperse aluminum nanoparticles with a core-shell structure near the ideal emitter can enhance ultraviolet luminescence emission at 380 nm by a factor of two and can amplify emission by up to 85 times for poor emitters with an intrinsic quantum yield of 0.01. It was established that an increase in particle size and broadening the particle size distribution lead to the growth of the Plasmon-enhancement factor. The selected synthesis technology is constrained by producing aluminum nanoparticles, within a narrow range of mean sizes specifically between 15 and 26 nm, which can be potentially extended to larger by in-flow laser sintering of agglomerates. However, it is important to emphasize the substantial advantage of spark discharge method, which lies in its excellent compatibility with dry aerosol printing technology. Our research group has already successfully developed methods for dry aerosol printing of UV-luminescence-enhancing structures based on aluminum nanoparticles. Thus, the results of the study lay the groundwork for further investigations aimed at engineering nanostructures based on polydisperse aluminum nanoparticles with precise size characteristics, which can be seamlessly incorporated into label-free chemical and biological sensors that exhibit ultraviolet luminescence.

Acknowledgments

The research was funded by the Russian Science Foundation project № 22-19-00311, https://rscf.ru/en/project/22-19-00311, as part of the research into the size, theoretical and experimental optical properties of Al nanoparticles and the Ministry of Science and Higher Education of the Russian Federation (state contract No. 075-03-2024-117, project identifier FSMG-2022-0036) as part of the synthesis of aluminum nanoparticles by spark discharge with different electrode diameters. We extend our sincere thanks to all those who contributed to preparing the instructions.

Author Contributuions

O.V.: formal analysis, investigation, writing—original draft preparation, visualization; A.L.: conceptualization, methodology, formal analysis, writing—original draft preparation, project administration, funding acquisition; E.K.: software; E.F.: investigation; A.S.: investigation, validation; A. N.: validation; M.N.: investigation; D.M.: data curation; E.K.: investigation; M.K.: resourses; Y.T.: validation, data curation; V.I.: writing—review and editing; supervision. All authors have read and agreed to the published version of the manuscript.

Conflicts of Interest

The authors declare no conflict of interest.

References

[1] X. Gao, C. Wang, W. Bai, Y. Hou, and D. Che, "Aluminum-based fuels as energy carriers for controllable power and hydrogen generation—A review," *Energies*, vol. 16, no. 1, p. 436, Dec. 2023, doi: 10.3390/en16010436.

[2] M. Y. Haller, D. Carbonell, M. Dudita, D. Zenhäusern, and A. Häberle, "Seasonal energy storage in aluminium for 100 percent solar heat and electricity supply," *Energy Conversion and Management: X*, vol. 5, Jan. 2020, Art. no. 100017, doi: 10.1016/j.ecmx.2019.100017.

[3] B. Aduev, Y. Kraft, D. Nurmukhametov, G. Belokurov, N. Nelubina, and Z. Ismagilov, "Hydrogen production by oxidation of aluminum nanopowder in water under the action of laser pulses," *International Journal of Hydrogen Energy*, vol. 48, pp. 22484–22494, Jul. 2023, doi: 10.1016/j.ijhydene.2023.03.096.

[4] M. H. Chowdhury, K. Ray, S. K. Gray, J. Pond, and J. R. Lakowicz, "Aluminum nanoparticles as substrates for metal-enhanced fluorescence in the ultraviolet for the label-free detection of biomolecules," *Analytical chemistry*, vol. 81, pp. 1397–1403, Jan. 2009, doi: 10.1021/ac802118s.

[5] S. K. Das, S. Mahapatra, and H. Lahan, "Aluminium-ion batteries: Developments and challenges," *Journal of Materials Chemistry A*, vol. 5, pp. 6347–6367, Jan. 2017, doi: 10.1039/c7ta00228a.

[6] Q. Hao, C. Wang, H. Huang, W. Li, D. Du, Di Han, T. Qiu, and P. K. Chu, "Aluminum plasmonic photocatalysis," *Scientific Reports*, vol. 5, Oct. 2015, Art. no. 15288, doi: 10.1038/srep15288.

[7] M. W. Knight, N. S. King, L. Liu, H. O. Everitt, P. Nordlander, and N. J. Halas, "Aluminum for plasmonics," *ACS Nano*, vol. 8, pp. 834–840, Dec. 2014, doi: 10.1021/nn405495q.

[8] A. A. Gromov, Y. I. Strokova, and A. A. Ditts, "Passivation films on particles of electroexplosion aluminum nanopowders: A review," *Russian Journal of Physical Chemistry B*, vol. 4, no. 1, pp. 156–169, Apr. 2010, doi: 10.1134/S1990793110010239.

[9] S. V. Gudkov, D. E. Burmistrov, V. V. Smirnova, A. A. Semenova, and A. B. Lisitsyn, "A mini review of antibacterial properties of Al_2O_3 nanoparticles," *Nanomaterials*, vol. 12, no. 15, Jul. 2022, Art. no. 2635, doi: 10.3390/nano12152635.

[10] M. A. Ansari, H. M. Khan, A. A. Khan, R. Pal, S. S. Cameotra, "Antibacterial potential of Al_2O_3 nanoparticles against multidrug resistance strains of Staphylococcus aureus isolated from skin exudates," *Journal of nanoparticle research*, vol. 15, pp. 1–12, Sep. 2013 doi: 10.1007/s11051-013-1970-1.

[11] V. Klimov, *Nanoplasmonics*. Florida: Jenny Stanford Publishing, 2013, doi: 10.1201/b15442.

[12] D. V. Guzatov, S. V. Gaponenko, and H. V. Demir, "Plasmonic enhancement of electroluminescence," *AIP Advances*, vol. 8, Jan. 2018, Art. no. 015324, doi: 10.1063/1.5019778.

[13] K. Khurana and N. Jaggi, "Localized surface plasmonic properties of Au and Ag nanoparticles for sensors: A review," *Plasmonics*, vol. 16, pp. 981–999, Feb. 2021, doi: 10.1007/s11468-021-01381-1.

[14] S. V. Gaponenko, *Introduction to Nanophotonics*. Cambridge, UK: Cambridge University Press, 2010.

[15] J. E. Jacak and W. A. Jacak, "Plasmonic enhancement of solar cells efficiency: material dependence in semiconductor metallic surface nano-modification," *Plasmonics*, vol. 7, p. 79113, Nov. 2018.

[16] H. Kaçuş, M. Biber, and Ş. Aydoğan, "Role of the Au and Ag nanoparticles on organic solar cells based on P3HT: PCBM active layer," *Applied Physics A*, vol. 126, no. 10, p. 817, Sep. 2020.

[17] B. Ashok, M. Umamahesh, N. Hariram, S. Siengchin, and A. V. Rajulu, "Modification of waste leather trimming with in situ generated silver nanoparticles by one step method," *Applied Science and Engineering Progress*, vol. 14, no. 2, Mar. 2021, pp. 236–246, doi: 10.14416/j.asep.2021.01.007.

[18] G. V. Naik, V. M. Shalaev, and A. Boltasseva, "Alternative plasmonic materials: beyond gold and silver," *Advanced materials*, vol. 25, pp. 3264–3294, Jun. 2013, doi: 10.1002/adma.201205076.

[19] P. Singh, Z. Yang, V. Viswanathan, and J. Stevenson, "Observations on the structural degradation of silver during simultaneous exposure to oxidizing and reducing environments," *Journal of Materials Engineering and Performance*, vol. 13, pp. 287–294, Jun. 2004, doi: 10.1361/10599490419261.

[20] A. Taguchi, Y. Saito, K. Watanabe, S. Yijian, and S. Kawata, "Tailoring plasmon resonances in

the deep-ultraviolet by size-tunable fabrication of aluminum nanostructures," *Applied Physics Letters*, vol. 101, p. 81110, Aug. 2012, doi: 10.1063/1.4747489.

[21] J. Hu, L. Chen, Z. Lian, M. Cao, H. Li, W. Sun, N. Tong, and H. Zeng, "Deep-Ultraviolet–Blue-Light Surface Plasmon Resonance of Al and Alcore /Al_2O_3shell in Spherical and Cylindrical Nanostructures," *The Journal of Physical Chemistry C*, vol. 116, pp. 15584–15590, Jul. 2012, doi: 10.1021/jp305844g.

[22] V. I. Borisov, A. A. Lizunova, A. K. Mazharenko, D. Malo, A. A. Ramanenka, I. A. Shuklov, and V. V. Ivanov, "Aluminum nanoparticles synthesis in spark discharge for ultraviolet plasmonics," *Journal of Physics: Conference Series*, vol. 1695, p. 12021, Dec. 2020, doi: 10.1088/1742-6596/1695/1/012021.

[23] S. Tian, O. Neumann, M. J. McClain, X. Yang, L. Zhou, C. Zhang, P. Nordlander, and N. J. Halas, "Aluminum nanocrystals: A sustainable substrate for quantitative SERS-Based DNA detection," *Nano letters*, vol. 17, pp. 5071–5077, Aug. 2017, doi: 10.1021/acs.nanolett.7b02338.

[24] Y. Gutiérrez, R. Alcaraz de la Osa, D. Ortiz, J. M. Saiz, F. González, and F. Moreno, "Plasmonics in the ultraviolet with aluminum, gallium, magnesium and rhodium," *Applied Sciences*, vol. 8, no. 1, p. 64, Jan. 2018, doi: 10.3390/app8010064.

[25] Z. Li, C. Li, J. Yu, Z. Li, X. Zhao, A. Liu, S. Jiang, C. Yang, C. Zhang, and B. Man, "Aluminum nanoparticle films with an enhanced hot-spot intensity for high-efficiency SERS," *Optics express*, vol. 28, pp. 9174–9185, Mar. 2020, doi: 10.1364/OE.389886.

[26] Y. Wang, H. Gao, Y. Liu, D. Li, B. Zhao, W. Liang, Y. Sun, and L. Jiang, "Large-scale controllable fabrication of aluminum nanobowls for surface plasmon-enhanced fluorescence," *Nano Research*, vol. 16, pp. 10131–10138, Jul. 2023, doi: 10.1007/s12274-023-5492-6.

[27] H. Ghorbani, "A review of methods for synthesis of Al nanoparticles," *Oriental Journal of Chemistry*, vol. 30, pp. 1941–1949, Dec. 2014, doi: 10.13005/ojc/300456.

[28] A. A. Lizunova, D. Malo, D. V. Guzatov, I. S. Vlasov, E. I. Kameneva, I. A. Shuklov, M. N. Urazov, A. A. Ramanenka, and V. V. Ivanov, "Plasmon-enhanced ultraviolet luminescence in colloid solutions and nanostructures based on aluminum and ZnO nanoparticles," *Nanomaterials*, vol. 12, p. 4051, Nov. 2022, doi: 10.3390/nano 12224051.

[29] J. A. Haber and W. E. Buhro, "Kinetic instability of nanocrystalline aluminum prepared by chemical synthesis; facile room-temperature grain growth," *Journal of the American Chemical Society*, vol. 120, no. 42, pp. 10847–10855, Oct. 1998, doi: 10.1021/ja981972y.

[30] M. Castilla, S. Schuermans, D. Gerard, J. Martin, T. Maurer, U. Hananel, G. Markovich, J. Plain, and J. Proust, "Colloidal Synthesis of Crystalline Aluminum Nanoparticles for UV Plasmonics," *ACS Photonics*, vol. 9, pp. 880–887, Mar. 2022, Art. no. 1615, doi: 10.1021/acsphotonics. 1c01615.

[31] M. J. McClain, A. E. Schlather, E. Ringe, N. S. King, L. Liu, A. Manjavacas, M. W. Knight, I. Kumar, K. H. Whitmire, H. O. Everitt, P. Nordlander, and N. J. Halas, "Aluminum nanocrystals," *Nano Letters*, vol. 15, pp. 2751–2755, Apr. 2015, doi: 10.1021/acs.nanolett.5b00614.

[32] A. Muravitskaya, A. Gokarna, A. Movsesyan, S. Kostcheev, A. Rumyantseva, C. Couteau, G. Lerondel, A.L. Baudrion, S. Gaponenko, and P. Adam, "Refractive index mediated plasmon hybridization in an array of aluminium nanoparticles," *Nanoscale*, vol. 12, pp. 6394–6402, Feb. 2020, doi: 10.1039/C9NR09393A.

[33] K. Thyagarajan, C. Santschi, P. Langlet, and O. J. F. Martin, "Highly improved fabrication of Ag and Al nanostructures for UV and nonlinear plasmonics," *Advanced Optical Materials*, vol. 4, pp. 871–876, Mar. 2016, doi: 10.1002/adom. 201500740.

[34] L. X. Qian, W. Li, Z. Gu, J. Tian, X. Huang, P. T. Lai, and W. Zhang, "Ultra-Sensitive β-Ga_2O_3 Solar-Blind Photodetector with High-Density Al@Al_2O_3 Core−Shell Nanoplasmonic Array," *Advanced Optical Materials*, vol. 10, Jun. 2022, Art. no. 2102055, doi: 10.1002/adom.202102055.

[35] J. L. Gottfried, D. K. Smith, C. C. Wu, and M. L. Pantoya, "Improving the explosive performance of aluminum nanoparticles with Aluminum Iodate Hexahydrate (AIH)," *Scientific reports*, vol. 8, p. 8036, May 2018, doi: 10.1038/s41598-018-26390-9.

[36] M. Gazanfari, M. Karimzadeh, S. Ghorbani, M. R. Sadeghi, G. Azizi, H. Karimi, N. Fattahi, and Z. Karimzadeh, "Synthesis of aluminium nanoparticles by arc evaporation of an aluminium cathode surface," *Bulletin of Materials*

Science, vol. 37, pp. 871–876, Jun. 2014, doi: 10.1007/s12034-014-0019-0.

[37] M. I. Lerner, A. S. Lozhkomoev, A. V. Pervikov, and O. V. Bakina, "Synthesis of Al–Al_2O_3 and Al–Aln nanoparticle composites via electric explosion of wires," *Russian Physics Journal*, vol. 59, pp. 422–429, Jul. 2016, doi: 10.1007/s11182-016-0789-5.

[38] A. A. Gromov, U. Förter-Barth, and U. Teipel, "Aluminum nanopowders produced by electrical explosion of wires and passivated by non-inert coatings: Characterisation and reactivity with air and water," *Powder Technology*, vol. 164, pp. 111–115, May 2006, doi: 10.1016/j.powtec. 2006.03.003

[39] R. S. Tabari, M. Halali, A. A Javadi, and M. H. Khanjanpour, "Experimental analysis and characterization of high-purity aluminum nanoparticles (Al-NPs) by electromagnetic levitation gas condensation (ELGC)," *Nanomaterials*, vol.10, pp. 111–115, Oct. 2020, doi: 10.3390/ nano10102084.

[40] W. Jang, H. Byun, and J. H. Kim, "Rapid preparation of paper-based plasmonic platforms for SERS applications," *Materials Chemistry and Physics*, vol. 240, p. 122124, Jan. 2020, doi: 10.1016/j.matchemphys.2019.122124.

[41] A. A. Ramanenka, S. V. Vaschenko, V. V. Stankevich, A. Y. Lunevich, Y. F. Glukhov, and S. V. Gaponenko, "Plasmonic enhancement of luminescence of fluorscein isothiocyanate and human immunoglobulin conjugates," *Journal of Applied Spectroscopy*, vol. 81, pp. 222–225, May 2014, doi: 10.1007/s10812-014-9913-x.

[42] A. R. Markelonis, J. S. Wang, B. Ullrich, C. M. Wai, and G. J. Brown, "Nanoparticle film deposition using a simple and fast centrifuge sedimentation method," *Applied Nanoscience*, vol. 5, pp. 457–468, Apr. 2015, doi: 10.1007/ s13204-014-0338-x.

[43] A. A. Efimov, P. V. Arsenov, V. I. Borisov, A. I. Buchnev, A. A. Lizunova, D. V. Kornyushin, S. S. Tikhonov, A. G. Musaev, M. N. Urazov, M. I. Shcherbakov, D. V. Spirin, and V. V. Ivanov, "Synthesis of nanoparticles by spark discharge as a facile and versatile technique of preparing highly conductive Pt nano-ink for printed electronics," *Nanomaterials*, vol. 11, p. 234, Jan. 2021, doi: 10.3390/nano11010234.

[44] A. Kohut, L. P. Villy, A. Kéri, Á. Bélteki, D. Megyeri, B. Hopp, G. Galbács, and Z. Geretovszky, "Full range tuning of the composition of Au/Ag binary nanoparticles by spark discharge generation," *Scientific Reports*, vol. 11, p. 5117, Mar. 2021, doi: 10.1038/s41598-021-84392-6.

[45] V. V. Ivanov, A. A. Efimov, D. A. Myl'nikov, and A.A. Lizunova, "Synthesis of nanoparticles in a pulsed-periodic gas discharge and their potential applications," *Russian Journal of Physical Chemistry A*, vol. 92, pp. 607–612, Mar. 2018, doi: 10.1134/S0036024418030093.

[46] V. Ivanov, A. Lizunova, O. Rodionova, A. Kostrov, D. Kornyushin, A. Aybush, A. Golodyayeva, A. Efimov, and V. Nadtochenko, "Aerosol dry printing for SERS and photoluminescence-active gold nanostructures preparation for detection of traces in dye mixtures," *Nanomaterials*, vol. 12, p. 448, Jan. 2022, doi: 10.3390/nano12030448.

[47] M. Slotte and R. Zevenhoven, "Energy efficiency and scalability of metallic nanoparticle production using arc/spark discharge," *Energies*, vol. 10, no. 10, p. 1605, Oct. 2017, doi: 10.3390/ en10101605.

[48] M. E. Messing, "The advantages of spark discharge generation for manufacturing of nanoparticles with tailored properties," *Journal of Green Engineering*, vol. 5, no. 3, pp. 83–96, Aug. 2016, doi: 10.13052/jge1904-4720.5346.

[49] N. S. Tabrizi, M. Ullmann, V. A. Vons, U. Lafont, and A. Schmidt-Ott, "Generation of nanoparticles by spark discharge," *Journal of Nanoparticle Research*, vol. 11, pp. 315–332, Feb. 2009, doi: 10.1007/s11051-008-9407-y.

[50] J. Feng, N. Ramlawi, G. Biskos, and A. Schmidt-Ott, "Internally mixed nanoparticles from oscillatory spark ablation between electrodes of different materials," *Aerosol Science and Technology*, vol. 52, pp. 505–514, May 2018, doi: 10.1080/02786826.2018.1427852.

[51] K. Khabarov, M. Nouraldeen, S. Tikhonov, A. Lizunova, A. Efimov, and V. Ivanov, "Modification of aerosol gold nanoparticles by nanosecond pulsed-periodic laser radiation," *Nanomaterials*, vol. 11, no. 10, p. 2701, Oct. 2021, doi: 10.3390/nano11102701.

[52] A. Lizunova, A. Mazharenko, B. Masnaviev, E. Khramov, A. Efimov, A. Ramanenka, I. Shuklov, and V. Ivanov, "Effects of temperature on the morphology and optical properties of spark discharge germanium nanoparticles," *Materials*, vol. 13, p. 4431, Oct. 2020, doi: 10.3390/ma13194431.

[53] K. Khabarov, M. Urazov, A. Lizunova, E. Kameneva, A. Efimov, and V. Ivanov, "Influence of Ag electrodes asymmetry arrangement on their erosion wear and nanoparticle synthesis in spark discharge," *Applied Sciences*, vol. 11, p. 4147, May 2021, doi: 10.3390/app11094147.

[54] J. Katyal and R. K. Soni, "Size- and shape-dependent plasmonic properties of aluminum nanoparticles for nanosensing applications," *Journal of Modern Optics*, vol. 60, pp. 1717–1728, Nov. 2013, doi: 10.1080/09500340.2013.856483.

[55] S. V. Gaponenko and D. V. Guzatov, "Colloidal plasmonics for active nanophotonics," *Proceedings of the IEEE*, vol. 108, pp. 704–720, May 2020, doi: 10.1109/JPROC.2019.2958875.

[56] A. A. Ramanenka, A. A. Lizunova, A. K. Mazharenko, M. F. Kerechanina, V. V. Ivanov, and S. V. Gaponenko, "Preparation and optical properties of isopropanol suspensions of aluminum nanoparticle," *Journal of Applied Spectroscopy*, vol. 87, no. 4, pp. 662–667, Sep. 2020, doi: 10.1007/s10812-020-01051-w.

[57] B. A. Russell, "Protein encapsulated gold nanoclusters for biological applications," Ph.D. Thesis, Department of Physics University of Strathclyde, Glasgow, Scotland, 2017, doi: 10.13140/RG.2.2.36594.40645.

[58] S. S. A. Tarek, S. B. Faruque, S. M. Sharafuddin, K. M. E. Hasan, A. K. M. M. Hossain, H. Ara, and Y. Haque, "Linear and thermo-optically generated nonlinear optical response of bovine serum albumin and its constituent amino acids in continuous wave z-scan," *AIP Advances*, vol. 13, no. 3, Mar. 2023, doi: 10.1063/5.0135447.

[59] S Liu, Y. Sun, L. Chen, Q. Zhang, X. Li, and J. Shuai, "A review on plasmonic nanostructures for efficiency enhancement of organic solar cells," *Materials Today Physics*, vol. 24, May 2022, Art. no. 100680, doi: 10.1016/j.mtphys.2022.100680.

[60] J. W. Lee, G. Ha, J. Park, H. G. Song, J. Y. Park, J Lee, and J. K. Kim, "AlGaN deep-ultraviolet light-emitting diodes with localized surface plasmon resonance by a high-density array of 40 nm Al nanoparticles," *ACS Applied Materials & Interfaces*, vol. 12, no. 32, pp. 36339–36346, Aug. 2020, doi: 10.1021/acsami.0c08916.

[61] R. Reinmann and M. Akram, "Temporal investigation of a fast spark discharge in chemically inert gases," *Journal of Physics D: Applied Physics*, vol. 30, no. 7, p. 1125, Apr. 1997, doi: 10.1088/0022-3727/30/7/010.

[62] D. Mylnikov, A. Lizunova, V. Borisov, S. Paranin, and V. Ivanov, "Germanium nanoparticles, synthesis in spark discharge," *Oriental Journal of Chemistry*, vol. 34, pp. 2677–2680, Oct. 2018, doi: 10.13005/ojc/340563.

[63] J. Feng, X. Guo, N. Ramlawi, T. V. Pfeiffer, R. Geutjens, S. Basak, H. Nirschl, G. Biskos, H. W. Zandbergen, and A. Schmidt-Ott, "Green manufacturing of metallic nanoparticles: A facile and universal approach to scaling up," *Journal of Materials Chemistry A*, vol. 4, pp. 11222–11227, 2016, doi: 10.1039/C6TA03221D.

[64] A. Efimov, I. Volkov, A. Varfolomeev, A. Vasiliev, and V. Ivanov, "Tin oxide nanoparticles produced by spark ablation: Synthesis and gas sensing properties," *Oriental Journal of Chemistry*, vol. 32, pp. 2909–2913, Dec. 2016, doi: 10.13005/ojc/320609.

[65] X. Xu, L. Li, W. Han, J. Luo, D. Zhang, Y. Wang, and G. Li, "Crystalline/amorphous Al/Al_2O_3 core/shell nanospheres as efficient catalysts for the selective transfer hydrogenation of α, β-unsaturated aldehydes," *Catalysis Communications*, vol. 109, pp. 50–54, May 2018, doi: 10.1002/slct.201904480

[66] Y. Lin, X. Q. Liu, T. Wang, C. Chen, H. Wu, L. Liao, and C. Liu, "Shape-dependent localized surface plasmon enhanced UV-emission from ZnO grown by atomic layer deposition," *Nanotechnology*, vol. 24, no. 12, Mar. 2013, Art. no. 125705, doi: 10.1088/0957-4484/24/12/125705.

[67] T. L. Temple and D. M. Bagnall, "Optical properties of gold and aluminium nanoparticles for silicon solar cell applications," *Journal of Applied Physics*, vol. 109, no. 8, Apr. 2011, doi: 10.1063/1.3574657.

[68] J. Gesner, M. L. Pantoya, and V. I. Levitas, "Effect of oxide shell growth on nano-aluminum thermite propagation rates," *Combustion and Flame*, vol. 159, no. 11, pp. 3448–3453, Nov. 2012, doi: 10.1016/j.combustflame.2012.06.002.

[69] M. T. Swihart, "Vapor-phase synthesis of nanoparticles," *Current Opinion in Colloid & Interface Science*, vol. 8, no. 1, pp. 127–133, Mar. 2003, doi: 10.1016/S1359-0294(03)00007-4.

[70] G. Maidecchi, G. Gonella, R. Zaccaria, R. Moroni, L. Anghinolfi, A. Giglia, S. Nannarone, L. Mattera, H.-L. Dai, M. Canepa, and F. Bisio, "Deep ultraviolet plasmon resonance in aluminum

nanoparticle arrays," *ACS Nano*, vol. 7, pp. 5834–5841, Jul. 2013, doi: 10.1021/nn400918n.

[71] J. M. Zook, V. Rastogi, R. I. Maccuspie, A. M. Keene, and J. Fagan, "Measuring agglomerate size distribution and dependence of localized surface plasmon resonance absorbance on gold nanoparticle agglomerate size using analytical ultracentrifugation," *ACS Nano*, vol. 5, pp. 8070–8079, Oct. 2011, doi: 10.1021/nn202645b.

[72] I. Tanabe, Y. Y. Tanaka, K. Watari, T. Hanulia, T. Goto, W. Inami, Y. Kawata, and Y. Ozaki, "Far- and deep-ultraviolet surface plasmon resonance sensors working in aqueous solutions using aluminum thin films," *Scientific Reports*, vol. 7, p. 5934, Jul. 2017, doi: 10.1038/s41598-017-06403-9.

[73] Y. Ekinci, H. H. Solak, and J. F. Löffler, "Plasmon resonances of aluminum nanoparticles and nanorods," *Journal of Applied Physics*, vol. 104, Oct. 2008, Art. no. 083107, doi: 10.1063/1.2999370.

[74] V. K. Pustovalov, and L. G. Astafyeva, "Influence of Shell Parameters on Optical Properties of Spherical Metallic Core-Oxide Shell Nanoparticles," *Journal of Nanomaterials*, vol. 2015, Jan. 2015, Art. no. 812617, doi: 10.U55/2015/812617.

[75] J. Katyal, and R. K. Soni, "Size-and shape-dependent plasmonic properties of aluminum nanoparticles for nanosensing applications," *Journal of Modern Optics*, vol. 60, pp. 1717–1728, Nov. 2013, doi: 10.1080/09500340.2013.856483.

[76] Y. Wei, Y. Gu, M. Zhao, Y. Dong, J. Chen, and H. Zeng, "Deep-Ultraviolet Plasmon Resonances in Al-Al_2O_3@C Core–Shell Nanoparticles Prepared via Laser Ablation in Liquid," *ACS Applied Electronic Materials*, vol. 2, pp. 802–807, Mar. 2020, doi: 10.1021/acsaelm.9b00851.

[77] A. L. Feng, M. L. You, L. Tian, S. Singamaneni, M. Liu, Z. Duan, T. J. Lu, F. Xu, and M. Lin, "Distance-dependent plasmon-enhanced fluorescence of upconversion nanoparticles using polyelectrolyte multilayers as tunable spacers," *Scientific Reports*, vol. 5, p. 7779, Jan. 2015, doi: 10.1038/srep07779.

[78] O. Kulakovich, N. Strekal, M. Artemyev, A. Stupak, S. Maskevich, and S. Gaponenko, "Improved method for fluorophore deposition atop a polyelectrolyte spacer for quantitative study of distance-dependent plasmon-assisted luminescence," *Nanotechnology*, vol. 17, pp. 5201–5206, Oct. 2006, doi: 10.1088/0957-4484/17/20/026.

[79] Q. T. Pham, G. L. Ngo, C. T. Nguyen, I. Ledoux-Rak, and N. D. Lai, "Unraveling the Dominant Size Effect in Polydisperse Solutions and Maximal Electric Field Enhancement of Gold Nanoparticles," *Photonics*, vol. 11, p. 691, Jul. 2024, doi: 10.3390/photonics11080691.

[80] D. Malo, A. A. Lizunova, O. V. Vershinina, E. M. Filalova, and V. V. Ivanov, "Ultraviolet photoluminescence enhancement of zinc oxide nanocrystals in colloidal mixtures with spark discharge aluminum nanoparticles," *St. Petersburg Polytechnic University Journal. Physics and Mathematics*, vol. 16, p. 443, Art. no. 3.2, 2023, doi: 10.18721/JPM.163.245.

[81] D. Hong, E. J. Jo, D. Bang, C. Jung, Y. E. Lee, Y. S. Noh, M. G. Shin, and M. G. Kim, "Plasmonic approach to fluorescence enhancement of mesoporous silica-coated gold nanorods for highly sensitive influenza A virus detection using lateral flow immunosensor," *ACS Nano*, vol. 17, pp. 16607–16619, Sep. 2023, doi: 10.1021/acsnano.3c02651.

[82] Y. Jeong, Y. M. Kook, K. Lee, and W. G. Koh, "Metal enhanced fluorescence (MEF) for biosensors: General approaches and a review of recent developments," *Biosensors & Bioelectronics*, vol. 111, pp. 102–116, Jul. 2018, doi: 10.1016/j.bios.2018.04.007.

[83] H. Huang, J. Lai, J. Lu, and Z. Li, "Performance enhancement of ZnO ultraviolet detector by localized surface plasmon resonance of Al nanoparticles," *Applied Physics A*, vol. 127, p. 679, Sep. 2021, doi: 10.1007/s00339-021-04820-2.

[84] S. Zhang, R. He, Y. Duo, R. Chen, L. Wang, J. Wang, and T. Wei, "Plasmon-enhanced deep ultraviolet Micro-LED arrays for solar-blind communications," *Optics Letters*, vol. 48, pp. 3841–3844, Aug. 2023, doi: 10.1364/OL.496397.